Pressure Fluctuation?Vorticity Interaction in the Volute of Centrifugal Pump as Hydraulic Turbines (PATs)

Authors:

Tong Lin, Jianrong Zhang, Jian Li, Xiaojun Li, Zuchao Zhu

Date Submitted: 2023-02-21

Keywords: pump as turbine, pressure pulsation, numerical simulation, flow characteristic, volute

Abstract:

The pump as turbines (PATs) has been widely used in the petrochemical, seawater desalination, and mining industries. Volutes are critical components for flow guidance and energy conversion in the PATs. Therefore, its inner flow characteristic could significantly influence the hydraulic turbine system stability. To reveal the vortex evolution, pressure pulsation characteristics, and the interaction between the two in the volute of PATs, a single-stage cantilever hydraulic turbine is investigated by the numerical and experiment method. The effect of impeller rotation on vorticity distribution and pressure fluctuation intensity in volute is analyzed based on the numerical simulation results. By clarifying the frequency components corresponding to local high amplitude vorticity and pressure pulsations, the relationship between vortex evolution and pressure pulsations is established. The results showed that the dominant frequency of pressure pulsation in the circumferential direction of the volute is 6fn under different operating conditions, and the pressure pulsation characteristics in the inlet section of the volute were less affected by the rotor?stator interaction. Under Qb and 1.3Qb conditions, the vorticity pulsation near the walls in the circumferential direction of the volute had less effect on local pressure pulsation characteristics. The evolution of vorticity at the leading edge of the volute tongue intensified the local pressure pulsations as the flow rate increased. Under 0.7Qb conditions, the vorticity pulsation characteristics in the volute are complex and have a relatively significant influence on local pressure pulsation.

Record Type: Published Article

Submitted To: LAPSE (Living Archive for Process Systems Engineering)

Citation (overall record, always the latest version):	LAPSE:2023.0769
Citation (this specific file, latest version):	LAPSE:2023.0769-1
Citation (this specific file, this version):	LAPSE:2023.0769-1v1

DOI of Published Version: https://doi.org/10.3390/pr10112241

processes

MDPI

Article

Pressure Fluctuation–Vorticity Interaction in the Volute of Centrifugal Pump as Hydraulic Turbines (PATs)

Tong Lin [1,2,3], Jianrong Zhang [1], Jian Li [1], Xiaojun Li [2] and Zuchao Zhu [2,*]

[1] Jiangxi College of Applied Technology, Ganzhou 341000, China
[2] National-Provincial Joint Engineering Laboratory for Fluid Transmission System Technology, Zhejiang Sci-Tech University, Hangzhou 310018, China
[3] Key Laboratory of Ionic Rare Earth Resources and Environment, Ministry of Natural Resources, Ganzhou 341000, China
* Correspondence: zhuzuchao@zstu.edu.cn

Abstract: The pump as turbines (PATs) has been widely used in the petrochemical, seawater desalination, and mining industries. Volutes are critical components for flow guidance and energy conversion in the PATs. Therefore, its inner flow characteristic could significantly influence the hydraulic turbine system stability. To reveal the vortex evolution, pressure pulsation characteristics, and the interaction between the two in the volute of PATs, a single-stage cantilever hydraulic turbine is investigated by the numerical and experiment method. The effect of impeller rotation on vorticity distribution and pressure fluctuation intensity in volute is analyzed based on the numerical simulation results. By clarifying the frequency components corresponding to local high amplitude vorticity and pressure pulsations, the relationship between vortex evolution and pressure pulsations is established. The results showed that the dominant frequency of pressure pulsation in the circumferential direction of the volute is $6f_n$ under different operating conditions, and the pressure pulsation characteristics in the inlet section of the volute were less affected by the rotor–stator interaction. Under Q_b and $1.3Q_b$ conditions, the vorticity pulsation near the walls in the circumferential direction of the volute had less effect on local pressure pulsation characteristics. The evolution of vorticity at the leading edge of the volute tongue intensified the local pressure pulsations as the flow rate increased. Under $0.7Q_b$ conditions, the vorticity pulsation characteristics in the volute are complex and have a relatively significant influence on local pressure pulsation.

Keywords: pump as turbine; pressure pulsation; numerical simulation; flow characteristic; volute

Citation: Lin, T.; Zhang, J.; Li, J.; Li, X.; Zhu, Z. Pressure Fluctuation–Vorticity Interaction in the Volute of Centrifugal Pump as Hydraulic Turbines (PATs). *Processes* **2022**, *10*, 2241. https://doi.org/10.3390/pr10112241

Academic Editor: Krzysztof Rogowski

Received: 21 September 2022
Accepted: 13 October 2022
Published: 1 November 2022

1. Introduction

Pump as turbines (PATs) is a piece of energy recovery equipment widely used in petrochemicals, desalination, mining, and other energy-consuming industries as a substitute for pressure-reducing valves to realize the pressure relief process [1–3]. Volute is the critical flow guidance and energy conversion component of the PATs, and its inner flow characteristics could significantly influence turbine system stability [4–6]. Therefore, it is necessary to deeply analyze the vortex structure and pressure pulsation characteristics in the volute of PATs under typical operating conditions. The results of this research could provide a reference for the performance improvement and operation regulation of PATs.

In recent years, scholars have concentrated on the research of flow characteristics and dynamic performance in the volute through theoretical analysis, numerical simulation, and experiments [7–9]. To improve the performance of PATs, Wang et al. designed a special impeller with forward-curve blades based on the theoretical analysis of the volute outflow condition and obtained the relationships among the volute constant, wrapping angle, and volute inlet dimension [10,11]. The outlet condition of the volute significantly influences the flow characteristic in its downstream flow components. Hence, Su et al. investigated the flow rate characteristics in typical volute sections of PATs through the

numerical method, and by the Lagrangian and Eulerian viewpoints they analyzed the unsteady flow characteristics of the inner volute [12]. They found that with increases in the volute section areas, the time-averaged velocity declined, and frequent bi-directional flow appeared in the volute outlet and the chamber inlet. Alessandro et al. investigated the effect of the volute tongue on the PATs performance using numerical and experimental methods, and the results showed that the new tongue model improved the hydraulic efficiency of PATs by 3.9% [13–15]. As traditional PATs lack the inlet flow control unit and the ability to improve the volute outlet conditions, many scholars have investigated the effects of stays and adjustable guide vanes to influence the inner flow characteristic of PATs [16–18]. Giosio et al. designed volute inlet flow control equipment to improve the efficiency of traditional PATs, and the results showed a maximum overall efficiency of 79%, in good agreement with PAT theory [19]. Shi et al. investigated the stay guide vane numbers to affect the performance of PATs, and numerical results showed that the hydraulic efficiency of the PATs improves by the assembly of the guide vanes at the volute outlet [20].

The radial asymmetric structure of the volute is the fundamental factor causing the pressure fluctuation and unbalanced radial force. Hence, investigating the unsteady flow generation and evolution mechanism is the key to proposing reasonable methods to improve the operational stability of the pump and PATs [21–23]. Santolaria et al., using the k–ε turbulence model, investigated the unsteady flow characteristic in the PATs, and the results showed that the radial force fluctuation was caused by the rotor–stator interaction [24]. Binama et al. compared the different blade trailing edge position influence on the pressure field of PATs under part-load conditions [25]. They indicated that the pressure fluctuation dominant frequency of the volute, impeller, and outlet pipe is the blade passing frequency and it could not obtain the relationships among the pressure pulsation variation and blade trailing edge position. Xiang et al. carried out an unsteady simulation that compared the pressure fluctuation characteristics of the PATs with the back-curved and front-curved impeller, and the results showed that the forward-curved impeller could effectively decrease the pressure fluctuation of the volute and improve the operation stability of the PATs [26]. Yang et al. researched the blade numbers, impeller diameter, and splitter blade influence on the pressure fluctuation characteristics of PATs systematically [27,28]. The results indicated that increasing the blade number and impeller diameter and adding the splitter blades could significantly decrease the unsteady pressure fluctuation of PATs. Gao et al. investigated the pressure and velocity distribution characteristic of the PATs under different operation conditions by the numerical method [29]. They found that the flow separation in the volute and impeller is generated by the local unsteady vortex.

Although the above references have made major progress in the research of the flow characteristics, pressure fluctuations, and vortex behaviors in the volute of PATs, the vortex-generated mechanism and its revolution effects on local pressure fluctuation characteristics in the volute of PATs are, however, still unclear, and few researchers have revealed the frequency components corresponding to local high amplitude vorticity and pressure pulsations in the volute. Therefore, the simulation and experimental methods are adopted in this paper to deeply reveal the vorticity–pressure fluctuation interaction characteristics in the volute. The results can be used to improve the stability of the operation and for further optimization of PATs. The main content of this paper is organized as follows: Section 2 describes the physical model and numerical methodology, and Section 3 compares the vorticity and pressure fluctuation intensity characteristics in the volute varied with flow rates and builds the relationship between vortex evolution and pressure fluctuations. Finally, Section 4 excerpts several valuable conclusions of this study.

2. Numerical Method

2.1. Physical Model

The model applied in the present study is a single stage cantilever pump as turbines (PATs) commonly used in the chemical industry with an n_s of 24.73. The designed flow, head, and rotating speed under the best efficiency point (BEP) of the pump were 45 m^3/h,

30.9 m, and 2900 rpm, respectively. The calculated model presented in Figure 1 includes an inlet duct, volute, impeller, impeller clearance, front chamber, back chamber, and outlet duct. The high-pressure fluid from the inlet pipe transports to the volute. The volute has two functions, the first being to convert some of the pressure energy of the fluid into mechanical energy, and the other to guide the water into the impeller. The impeller is the core component of energy conversion; the high-pressure and high-velocity fluid impacts the blade to push it to rotate. The outlet duct is the only outlet flow component of the PATs. To decline the impeller's radical force, the structure of the back and front chambers should be carefully designed. In order to accurately capture the true flow in the PATs, the wear ring clearance of the front and back chambers were structured. Table 1 presents the main geometric parameters of the PAT.

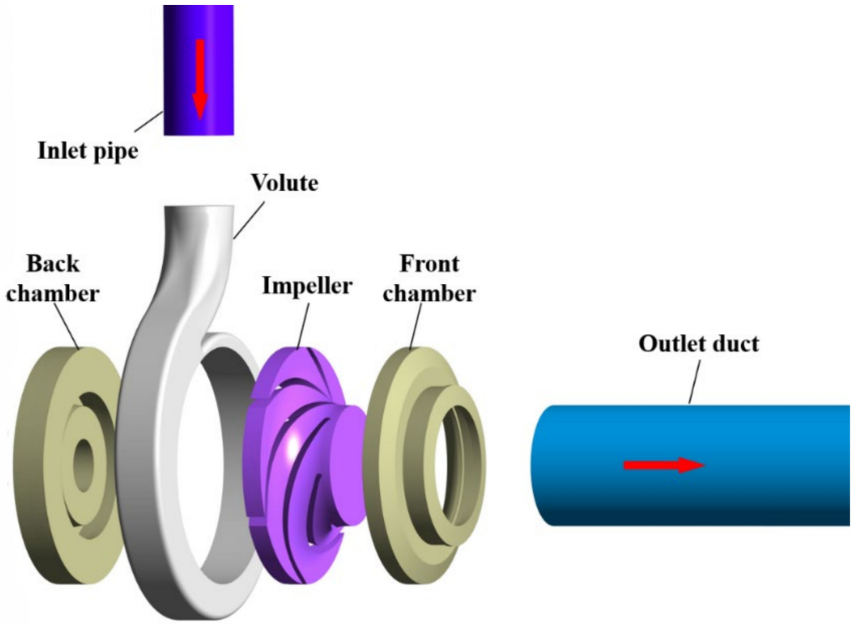

Figure 1. Calculation model of the PATs.

Table 1. Main geometric parameters of the PATs.

Parameter	Notation	Value	Parameter	Notation	Value
Impeller inlet diameter (mm)	D_1	169	Blade inlet angle (°)	β_2	25
Impeller outlet diameter (mm)	D_2	86	Blade outlet angle (°)	β_1	30
Impeller inlet width (mm)	b_1	14	Volute base circle diameter (mm)	D_3	172
Impeller outlet width (mm)	b_2	20	Blade number	Z	6

2.2. Governing Equations and Turbulence Model

The mass and momentum conservation equations were used to determine the velocity and pressure distribution in the PATs, regardless of the temperature and density variations of the flow medium in the simulations. The Reynolds averaged method was applied to the governing equations in the present study, and mass conservation and conservation of momentum are written as follows [30,31]:

Mass conservation:

$$\frac{\partial \overline{u}_i}{\partial x_i} = 0 \tag{1}$$

Conservation of momentum:

$$\frac{\partial \overline{u}_i}{\partial t} + \frac{\partial}{\partial x_j}\left(\overline{u}_i \overline{u}_j\right) = -\frac{1}{\rho}\frac{\partial \overline{p}}{\partial x_i} + \frac{1}{\rho}\frac{\partial}{\partial x_j}\left(\mu \frac{\partial \overline{u}_i}{\partial x_j} - \rho \overline{u_i' u_j'}\right) + f_i \tag{2}$$

where x_i and x_j are coordinate components; f_i is the body force component; $\overline{u}_i$ and $\overline{u}_j$ are time-averaged velocity components in cartesian coordinates; and ρ, $\overline{p}$, and $\rho\overline{u_i'u_j'}$ are density of flow medium, time-averaged pressure, and Reynolds stress tensor, respectively.

The flow characteristics are extremely complicated due to the high rotating speed of the impeller domain and distortion in flow channels. To precisely predict the hydraulic performance of PATs variation with the flow rates, the Shear Stress Transport (SST) k–ω turbulence model was selected to close the Reynolds-averaged governing equations under the steady calculation [32–34]. The SST k–ω turbulence model equations are shown in the following:

Turbulent kinetic energy equation:

$$\frac{\partial(\rho k)}{\partial t} + \frac{\partial\left(\rho k u_j\right)}{\partial x_j} = P_k + \frac{\partial}{\partial x_j}\left[\left(\mu + \frac{\mu_t}{\sigma_{k3}}\right)\frac{\partial k}{\partial x_j}\right] - \frac{\rho k^{3/2}}{l_{k-\omega}} \tag{3}$$

Turbulent frequency equation:

$$\frac{\partial(\rho\omega)}{\partial t} + \frac{\partial}{\partial x_j}\left[\rho\omega u_j - \left(\mu + \frac{\mu_t}{\sigma_{\omega 3}}\right)\frac{\partial\omega}{\partial x_j}\right] = \alpha_3\frac{\omega}{k}P_k - \beta_3\rho\omega^2 + 2\rho(1-F_1)\frac{1}{\omega\sigma_{\omega 2}}\frac{\partial k}{\partial x_j}\frac{\partial\omega}{\partial x_j} \tag{4}$$

where P_k is the production term of the equations; F_1 is the blending function used to switch the turbulence model between k–ω and k–ε based on the distance of a node to the nearest wall; μ is the dynamic viscosity; μ_t is the turbulence viscosity, and σ_{k3}, $\sigma_{\omega 3}$, α_3, β_3, and $\sigma_{\omega 2}$ are the model constants. $l_{k-\omega}$ in the second term on the right side of Equation (3) is the turbulence scale, which is defined as

$$l_{k-\omega} = k^{1/2}\omega\beta_k \tag{5}$$

The DES turbulence model based on the SST k–ω turbulence model (SST–DES) was applied to solve the Reynolds-averaged governing equations under the unsteady calculation to better capture the vortex distribution and evolution characteristics in the PAT. In the SST–DES turbulence model, the term of min ($l_{k-\omega}$, $C_{DES}\Delta$) was used to replace $l_{k-\omega}$. C_{DES} is the empirical constant with values of 0.61, and Δ is defined as Δ = max (Δx, Δy, Δz), which represents the largest mesh element dimension. When $l_{k-\omega} \geq C_{DES}\Delta$, the LES model was applied; otherwise, the SST k–ω model was used.

Due to the blade with the distortion structure, to truly reflect the details of the inner flow of the impeller, the correction coefficient f_r proposed by Spalart and Shur [35] considering the effects of curvature is used to modify the production term in the SST k–ω model and SST–DES models.

$$P_t = f_r \cdot P_t \tag{6}$$

where $f_r = \frac{2r^*}{1+r^*}(1+c_{r1})\left[1 - c_{r3}\tan^{-1}(c_{r2}\widetilde{r})\right] - c_{r1}$. c_{r1}, c_{r2}, c_{r3} are constants that are equal to 1, 2, and 1, respectively, and $\widetilde{r}$ and r^* are functions of the strain rate and system rotation, respectively.

2.3. Numerical Schemes and Boundary Conditions

The 3D steady-state incompressible simulation of PATs under the flow rates from 34.3 m^3/h to 101.8 m^3/h conditions, which correspond to $0.43Q_b$ to $1.3Q_b$ was performed in ANSYS CFX 2022 R2. The grid frame change models of the static domain connecting to the static domain and rotating domain were set to none and frozen rotor with the General Grid Interface mesh connection method, respectively. All the flow domains were set to stationary domains except the impeller. The rotating speed of the impeller was 2900 rpm, and multiple frames of reference were adopted in the simulation. The fluid energy transport medium was pure water with a density and temperature of 998.2 kg/m^3 and 25 °C, respectively. The high-resolution advection scheme and implicit second-order backward Euler scheme were applied to the discretization of convective terms and time

discretization of the momentum equations, respectively. Mass flow rate condition were in the position of the outlet, and the total pressure boundary was set as the inlet condition with a medium turbulence intensity of 5%. By changing the mass flow rate of the outlet, the flow characteristics and hydraulic performance of PATs under different operation conditions can be obtained. The convergence criterion of continuity and momentum equations is a root mean square (RMS) below 10^{-5}.

The steady simulation results of PATs solved by the SST k–ω turbulence model were used as the initial data for transient simulation to promote the convergence rate. Under the transient simulation, the time step was set to 5.7471×10^{-5} s, corresponding to one degree of impeller rotation, and the total time was set to 0.62068965 s, corresponding to the time needed for 30 revolutions of the impeller. The high-resolution discretization type was selected in the advection scheme, and the transient term was selected in the second-order backward Euler scheme. The interface between the impeller and the static domains adopted the frozen rotor interface in the steady simulation, and the transient rotor–stator model was selected for transient simulation. The convergence condition of all residuals was an RMS less than 1×10^{-6} under the transient simulation. The transient simulation results of the last five revolutions of the impeller were adopted to investigate the variations of pressure and vorticity in the volute with time. The monitoring points in the volute are shown in Figure 2.

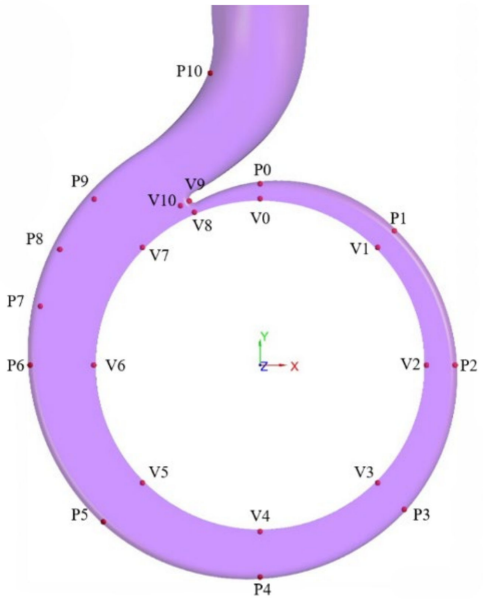

Figure 2. Monitoring points in the volute.

2.4. Mesh Generation and Sensitivity Analysis

Figure 3 shows the calculation mesh information of PATs' main flow domains. For precise capture of the detailed flow characteristics near the wall and to meet the values of the y+ requirement of the turbulence model, the methodology of local mesh refinement was adopted to build the boundary layer. Six different numbers of grids were created through an identical meshing method, and the node number increased from 2.54×10^6 to 9.43×10^6. The head of PATs under the BEP condition was selected as the criterion of grid independence. Figure 4 plots the variation curves of the head with the number of grid nodes increased. It indicates that when the grid number is larger than 6×10^6, the head and efficiency fluctuation of the PATs is not more than 0.5%. Considering the numerical accuracy and the ability of computational resources, the grid number of 7.25×10^6 was preliminarily selected.

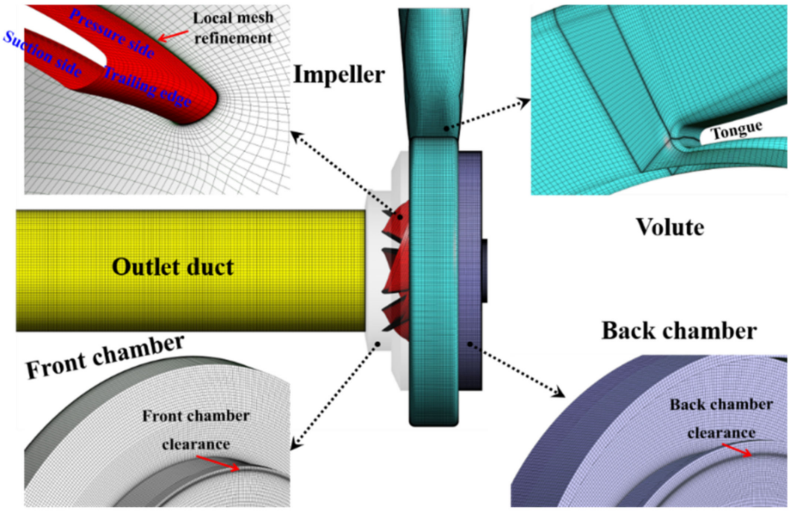

Figure 3. Grids of computational domains.

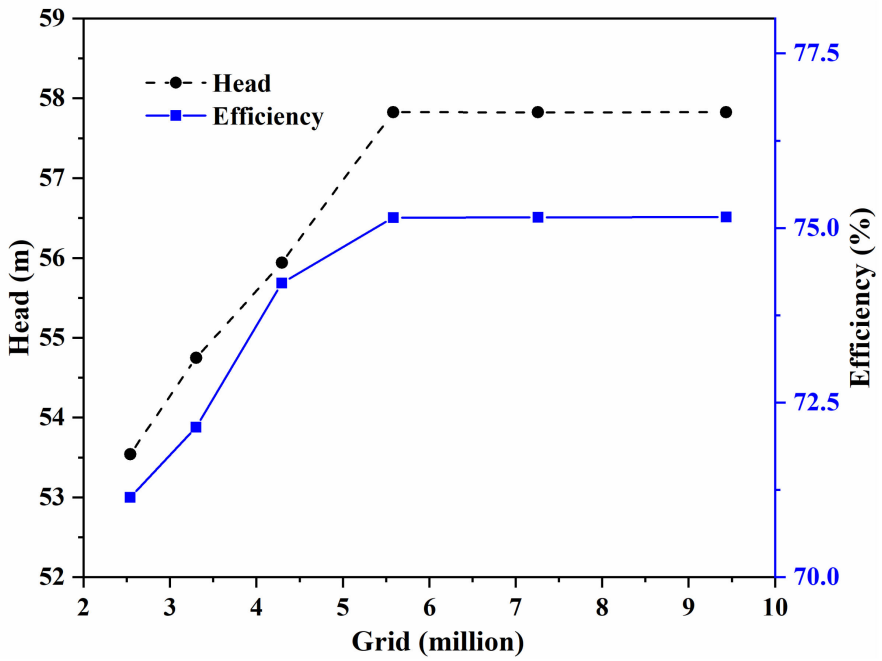

Figure 4. Grid independence verification.

To further verify the grid independence, the Grid Convergence Index (GCI) method was used, which is based on the Richardson extrapolation method, which was proposed by Roache and recommended by the Fluids Engineering Division of the American Society of Mechanical Engineers [36,37]. Three groups of mesh (N_1, N_2, N_3) were used to check the grid independence, and the number of nodes was 9.43×10^6, 7.25×10^6, and 5.58×10^6, respectively. The head and torque of PATs under the BEP condition were chosen to evaluate the grid error parameters. Table 2 presents the discretization errors of mesh cases. The discretization error of the mesh shows that the approximate relative error (e_a^{21}, e_a^{32}), extrapolated relative error (e_{ext}^{21}, e_{ext}^{32}), and fine-grid convergence index (GCI_{fine}^{21},GCI_{fine}^{32}) of head and efficiency were below 1.5%, which indicated that the mesh group of N2 could ensure the accuracy of the calculation. Finally, the mesh group with 7.25×10^6 nodes was selected for the simulation research in the present study. The mesh information for each domain is shown in Table 3.

Table 2. Computed discretization errors in head and efficiency.

	r_{21}	r_{32}	p	φ_{ext}^{21}	e_a^{21}	e_{ext}^{21}	GCI_{fine}^{21}	φ_{ext}^{32}	e_a^{32}	e_{ext}^{32}	GCI_{fine}^{32}
H (m)	1.32	1.31	0.986	57.83	0.0032%	0.0104%	1.30%	57.82	0.0024%	0.0079%	0.99%
η (%)	1.32	1.31	4.943	75.16	0.0014%	0.0005%	0.06%	75.16	0.0052%	0.0019%	0.23%

Table 3. Mesh information of each domain.

Domain	Node (Million)	Wall Average $y+$	Worst Quality
Inlet duct	0.3415	3.24	0.88
Volute	2.6914	6.37	0.52
Impeller	2.7624	6.24	0.43
Front chamber	0.4764	5.54	0.74
Back chamber	0.6213	4.84	0.72
Outlet duct	0.3649	3.76	0.87

2.5. Validation of Numerical Results

To verify the accuracy of the head and efficiency predicted by numerical methods, the hydraulic performance test of PATs was conducted by Hangzhou Dalu Industry Co., Ltd. (Hangzhou, China). Figure 5a shows the hydraulic performance test system of PATs, which comprises the water tank, control valve, feed pump, data acquisition and processing system, pressure transducer, electromagnetic flowmeter, electric eddy current dynamometer (ECD), PATs, and connecting pipe. The feed pump provides the hydraulic energy to drive the working PATs, and the ECD consumes the mechanical energy produced from the PATs. The ECD directly connects to the PATs by the flexible coupling with a coaxiality error below 0.1 mm, and the real-time data of rotating speed and torque are stored in its supporting software. Through coordinated regulation of the ECD, the control valve at the mainstream, and the bypass pipe, the hydraulic performance of PATs under the different operating conditions is obtained. The uncertainty of the pressure transducer, electromagnetic flowmeter, torque, and rotating speed sensor are ±0.2%, ±0.1%, and ±0.05%, respectively. The head and efficiency of PATs are calculated as follows.

$$H = \left(z_1 + \frac{p_1}{\rho g} + \frac{v_1^2}{2g}\right) - \left(z_2 + \frac{p_2}{\rho g} + \frac{v_2^2}{2g}\right) \tag{7}$$

$$\eta = \frac{\pi n T}{30 \rho g Q H} \times 100\% \tag{8}$$

where T is the torque of PATs; and z, p, and v are the vertical height, manometer pressure, and average velocity of cross section, respectively. The subscripts 1 and 2 represent inlet and outlet, respectively.

To verify the accuracy of the unsteady characteristics of PAT obtained by the simulation, four high frequencies dynamic pressure sensors were arranged in the volute in the test, and its position was consistent with the numerical setting. The physical model of PATs is presented in Figure 5b. As the experimental results obtained had a certain random error, the multiple repeated experimental results were used to calculate the performance parameter uncertainty of PATs. The uncertainty of flow rate, efficiency, and head were ±0.03%, ±0.13%, and ±0.14%, respectively. The uncertainty calculation formula is as follows:

$$S_x = \sqrt{\frac{1}{n}\left[\sum_{i=1}^{n}(x_i - \overline{x})^2\right]} \tag{9}$$

$$U_R = \pm \frac{t_{n-1} S_x}{\overline{x}\sqrt{n}} \times 100\% \tag{10}$$

where x_i, $\overline{x}$, n, S_x, and U_R are measurement value, average measurement value, measurement times, standard deviation, and random uncertainty, respectively. t_{n-1} is the confidence coefficient, which is equal to 0.95.

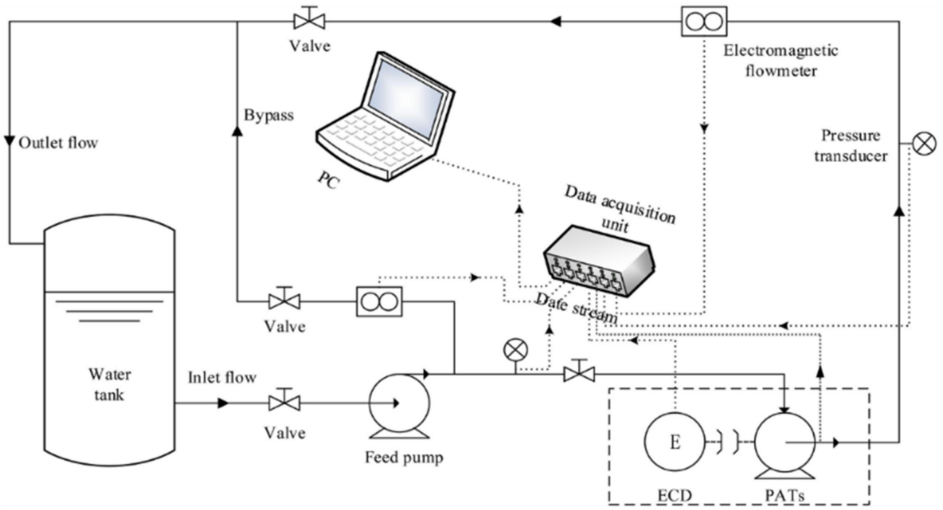

(**a**) Schematic of PATs hydraulic and dynamic characteristics test system

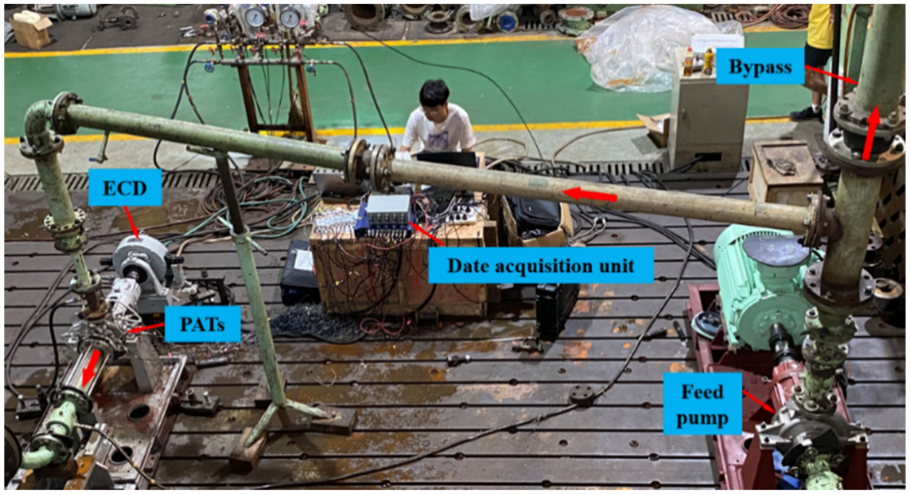

(**b**) PATs test site

Figure 5. PATs test system.

Figure 6 depicts the head and efficiency versus flow rate curve of the PATs comparison between that obtained by the CFD and the experimental method. The variation of head and efficiency with the flow rate were basically consistent in these two methods. As the flow rate increased, the head continually increased, while the efficiency increased at first and then decreased. The highest efficiency of PATs was reached at the flow rate of 78.3 m^3/h; under this operating condition, the head and efficiency predicted by the CFD method were 57.82 m and 75.15%, respectively. The prediction errors of efficiency and head were 2.47% and 4.91%, respectively.

The pressure fluctuations frequency domain signal of the volute obtained by CFD and test are compared in Figure 7. The pressure fluctuations coefficient P' is defined in Equation (11) to evaluate the intensity of pressure fluctuations [24]. At different positions in the circumferential direction of the S1 plane, the dominant frequency of pressure fluctuation predicted by CFD is 289.84 Hz, respectively, and the calculation error is −0.056% compared with the theoretical blade passing frequency (BPF). The amplitude of the dominant frequency of pressure fluctuation obtained by CFD and testing were well-matched, and the

values of P' were relatively large at the harmonic frequency of BPF, which indicated that the pressure fluctuations characteristic of volute main were affected by the rotor–stator interactions. As the pressure sensors showed a higher sampling frequency than the CFD, and the test results were affected by the pressure fluctuation of the feed pump, voltage variation of ECD, etc., the frequency components obtained by experiments were more diverse. Overall, the CFD prediction errors for both the hydraulic performance and pressure fluctuations characteristic of PATs were acceptable. Therefore, it can be concluded that the numerical simulation strategies adopted in the present study are dependable.

$$P' = 2(p - \overline{p})/\rho u_1^2 \tag{11}$$

where p, $\overline{p}$, and u_1 represent the stable pressure, average pressure, and circumferential velocity, respectively, of the impeller inlet.

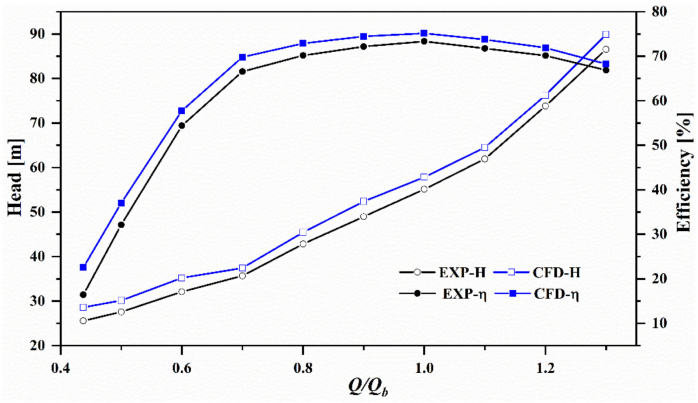

Figure 6. Hydraulic performance characteristics comparison between CFD and experiment.

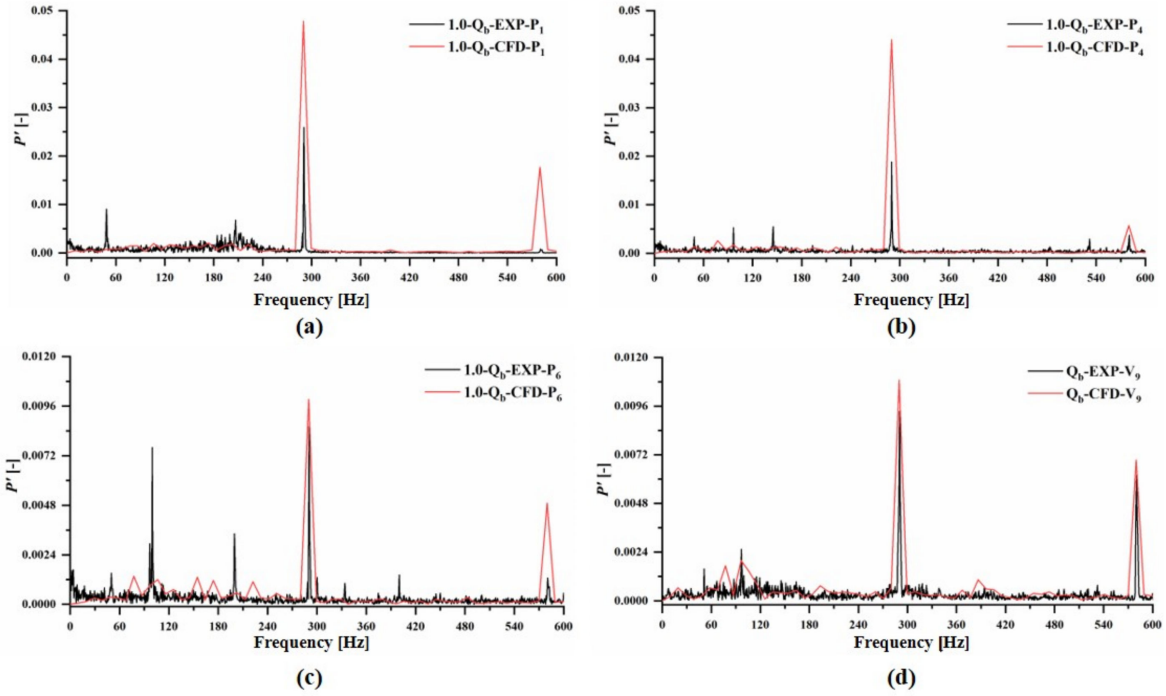

Figure 7. Pressure fluctuations frequency domain signal comparison between CFD and test. (**a**) pressure fluctuations coefficient of P1; (**b**) pressure fluctuations coefficient of P4; (**c**) pressure fluctuations coefficient of P6; (**d**) pressure fluctuations coefficient of V9.

3. Results and Discussion

3.1. Spatial and Temporal Evolution of the Vorticity

Figure 8 compares the vorticity distribution in the Z = 0 plane of the volute at the initial state for blade B1 under different operating conditions. The initial state is defined as the blade B1 leading-edge position aligns with the tongue of the volute. The dimensionless parameter ω* is defined in Equation (12) to evaluate the intensity of vorticity. It can be seen from the figure that the vorticity concentration regions in the volute were not changed with the varied flow rate. The vorticity in the volute concentrated near the walls and the tongue leading edge, as the fluid was affected by the strongly wall shear effect. In addition, influenced by the volute structure, the vortex near the walls of the volute throat (in region A) was shedding and propagated downstream. The vorticity value gradually decreased during the vortex position close to the outlet of the volute. As the outlet backflow of the volute, the vortex appeared at the partial interface between the volute and impeller, which caused the vorticity increases.

$$\omega^* = \omega/\omega_{\max} \tag{12}$$

where $\omega_{\max}$ is the maximum vorticity in the Z = 0 plane of the volute.

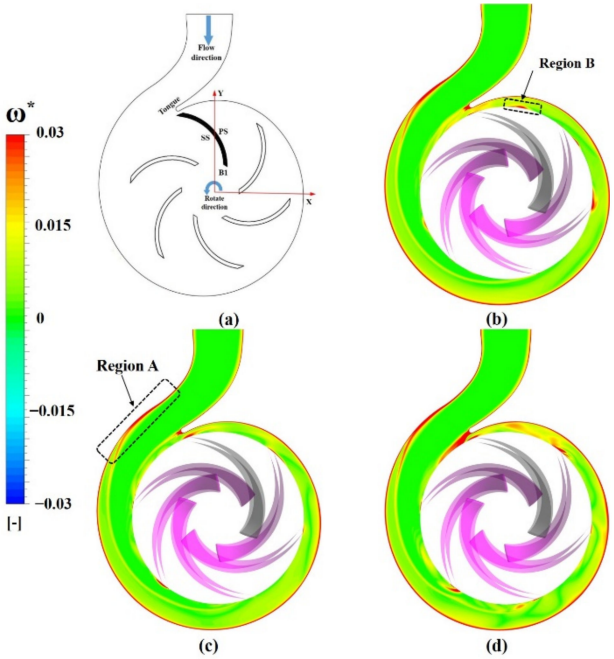

Figure 8. Spatial distribution of vorticity in the volute. (**a**) Diagram of the volute and impeller; (**b**) 0.7 Q_b; (**c**) Q_b; (**d**) 1.3 Q_b.

To investigate the impeller rotating affect to the spatial distribution of vorticity in the volute, the spatial and temporal evolution of the vorticity under the Q_b operation condition of B1 in one rotating cycle is shown in Figure 9. On the whole, vorticity concentration regions in the volute Z = 0 plane did not change with the time variation. However, there were large vorticity values at the outlet position of the sixth section of the volute and near the volute tongue at every moment under the Q_b operation condition. To interpret this phenomenon combined with the local flow characteristic in the volute, the backflow behavior at the interface of volute and impeller was evaluated by the flow deviation ratio (FDR). The FER is defined in Equation (13). The large values of FDR indicated that the flow deviated from the average flow in the impeller passage.

$$\mathrm{FDR} = \frac{(m - \overline{m})}{\overline{m}} \times 100\% \tag{13}$$

where m and $\overline{m}$ are the mass flow in the different impeller passages and the average mass flow in the whole impeller passage, respectively.

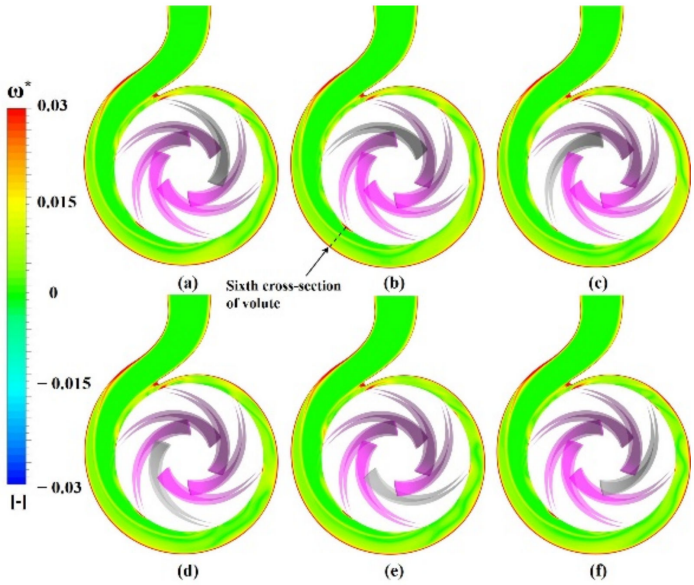

Figure 9. Spatial and temporal evolution of the vorticity under Q_b operation conditions. (**a**) 0 T; (**b**) 1/6 T; (**c**) 2/6 T; (**d**) 3/6 T; (**e**) 4/6 T; (**f**) 5/6 T.

Figure 10 compares the flow deviation ratio of different impeller passages with varied flow rate. With the flow rate increased, the FDR declined in most of the impeller passages, and the maximum value of FDR was less than 10% under the $1.3Q_b$ operation condition. The FDR is the most serious of all impeller passages under the no-load operation condition of PATs, in which the maximum value of FDR in the I1 is close to −90%. At Q_b operation conditions, the FDR of passages of I1 and I5 are larger than other passages, which causes the backflow to appear in those interfaces and increase the local vorticity.

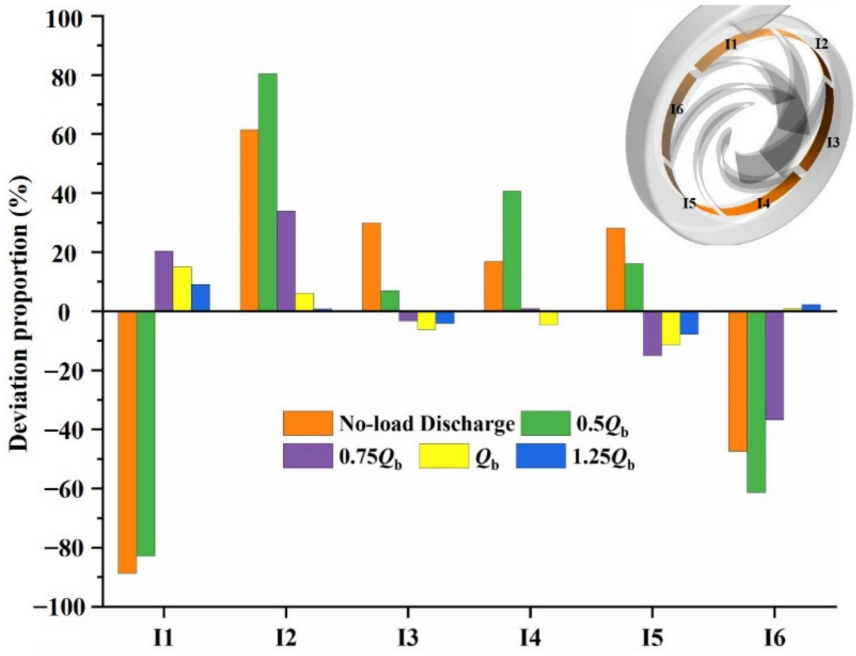

Figure 10. Flow deviation ratio in the different impeller passages.

Figure 11 shows the vorticity variation of monitoring points V9 with the impeller rotating, the lowercase letters (a to f) represent the circumferential direction position of the B1 impeller and correspond to the vorticity of monitoring points V9. The results indicated that the vorticity variation with periodicity and the number of vorticity wave peaks was equal to the number of blades. Six representative moments of blade B1 were used to determine that the effect of impeller rotation influenced the vorticity evolution near the volute tongue. That is, the vorticity was relatively large when the leading edge of blade aligned with the volute tongue and decreased with the blade away from the tongue. The variation of vorticity in one period corresponded to the processing of vortex shedding and regeneration.

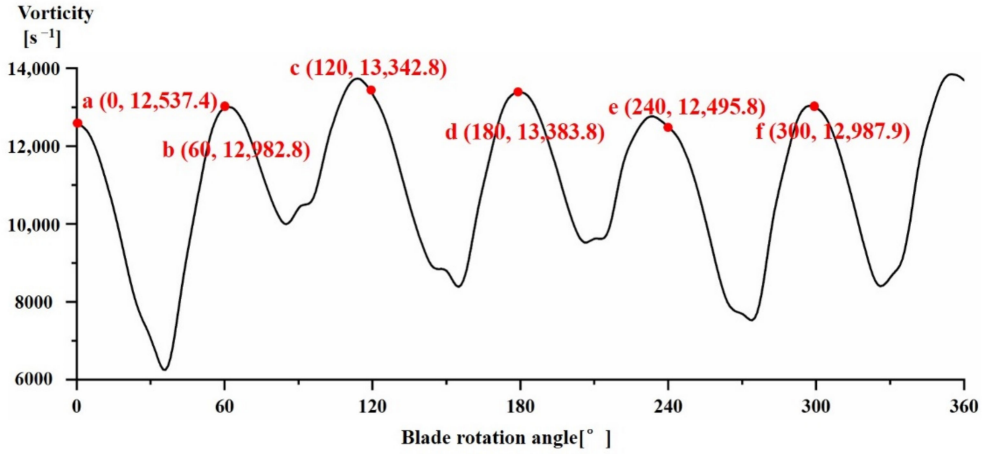

Figure 11. Vorticity of monitoring point V9 variation with time.

To further analyze the impeller rotating effect on the vortex evolution at the volute tongue leading edge, Figure 12 illustrates the comparison of Z-direction vorticity at this position in the 1/6 impeller rotating period under the Q_b operation condition. As shown in Figure 12a, a couple of vortexes with an opposite rotating direction appeared at the volute tongue leading edge. With the leading edge of the blade closing to the volute tongue, the vortex length developed, and the maximum vortex length appeared when the leading edge of the blade aligned with the volute tongue. With the impeller rotating away from the volute tongue, as shown in Figure 12d, the vortex began to shed and propagate downstream. While the blade B1 rotating degree θ was 30°, the vortex length at the volute tongue leading edge was the shortest, which indicated that the vortex arrived at inception status and moved to the next evolution period. Combined with Figures 11 and 12, it can be concluded that the blade rotation has a significantly influence on the vortex evolution characteristics at the volute tongue leading edge.

3.2. Vorticity Fluctuation Characteristics

To further analyze the vortex evolution effect on the local pressure and to reveal the sources for the frequency component of pressure fluctuation, the vorticity and pressure signal of the volute in the impeller's last five revolutions were analyzed by the Fast Fourier Transform algorithm. As shown in Figure 13, the vorticity fluctuation dominant frequency in the volute was composed of the blade pass frequency ($6f_n$), and the twice shaft frequency ($2f_n$), of which the dominant frequency of monitoring points P3 to P8 was $2f_n$, and the other monitoring points were $6f_n$, in which the f_n was impeller rotation frequency. The vorticity fluctuation amplitude of P10 was small, indicating that the flow inner the volute inlet contraction section was stable. The vorticity fluctuation amplitude of other monitoring points was relatively high, and the frequency components were more diverse under the low frequency band. From the position of monitoring points and its vorticity fluctuation dominant frequency, it can be inferred that the vortex evolution at the P3 to P8 was determined by the local flow characteristic affected by the volute structure and

flow rate, while the effect of rotor–stator interaction was the dominant contribution to the vorticity fluctuation of P0, P1, P2, P9, V9, and V10. The vorticity fluctuation amplitude of the monitoring points near the volute tongue was higher than those points near the walls, and closer to the volute tongue the amplitude was greater.

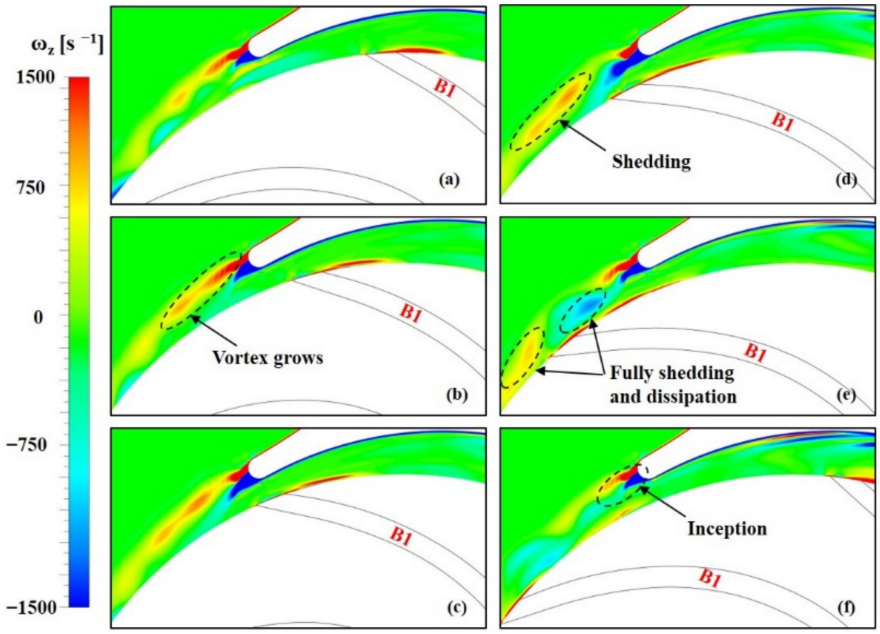

Figure 12. Z-direction vorticity at volute tongue leading edge in the 1/6 impeller rotating periods under the Q_b operation condition. (**a**) −18°; (**b**) −6°; (**c**) 0°; (**d**) 6°; (**e**) 18°; (**f**) 30°.

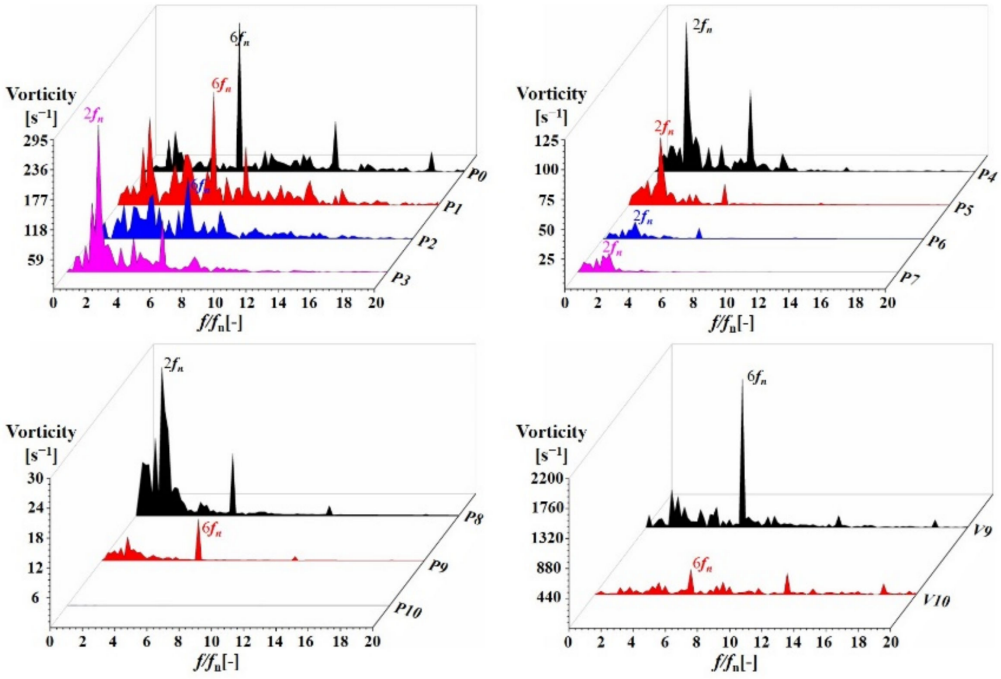

Figure 13. Frequency domain of vorticity fluctuation at the Q_b operation condition.

Figure 14 illustrates the vorticity fluctuation frequency domain of the volute at the $0.7Q_b$ operation condition. With the flow rate decreasing, the amplitude of vorticity fluctuation decreased, and its maximum values region also appeared near the leading edge of the volute tongue. The impact of the rotor–stator interaction on the vortex evolution

near the volute walls was weakened comparing to the Q_b condition. The reasons for this phenomenon may be the flow rate of PAT under the part load operation condition being close to its best efficiency points of pump condition. Therefore, it can be concluded that the flow rate and structure of the volute determine the vortex evolution behavior near the volute walls. As the position of monitoring points approached the volute inlet, the impeller rotating effect played a leading role in its vorticity fluctuation rather than the local flow characteristics. As seen in Figure 14, the vorticity fluctuation dominant frequency of P0 to P6 and P7 to P9 was $0.6f_n$ and f_n, respectively. In addition, though the P0 was located in the small pass-flow section of the volute, its vorticity fluctuation amplitude was relatively low due to the local flow characteristic of it being better under the $0.7Q_b$ operation condition. The vorticity fluctuation frequency components at the volute tongue leading edge under the $0.7Q_b$ condition was more diverse than the Q_b operation condition. The vorticity fluctuation dominant frequencies of V9 and V10 were $0.4f_n$ and $0.6f_n$, respectively.

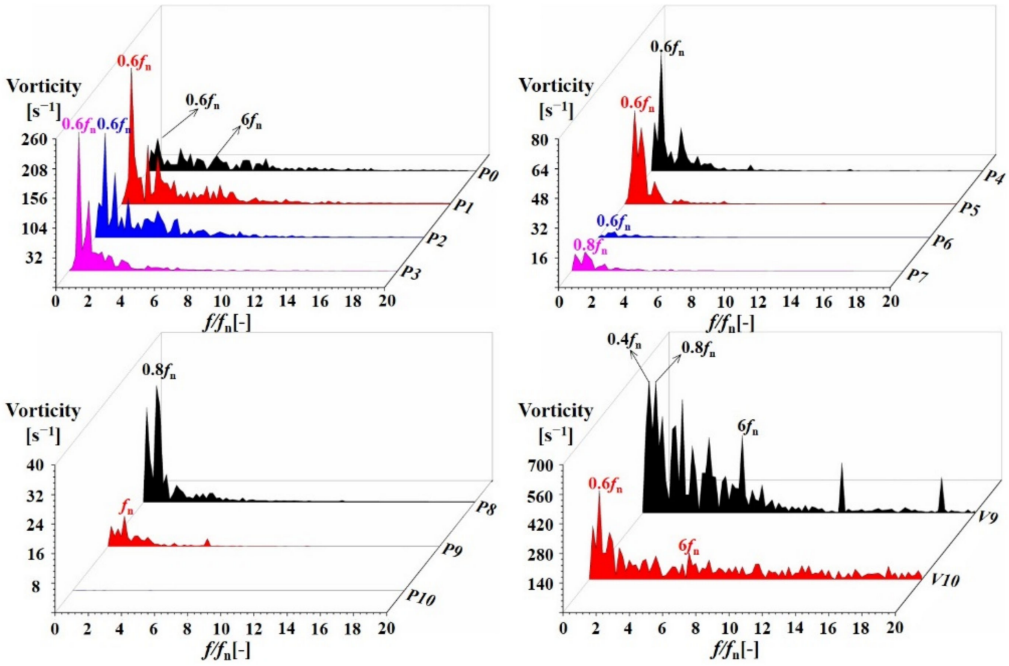

Figure 14. Frequency domain of vorticity fluctuation at the $0.7Q_b$ operation condition.

Figure 15 shows the frequency domain of vorticity fluctuation at the $1.3Q_b$ operation condition. Except for at P6 and P7, the dominant frequency of the monitoring points located at the volute circumferential direction was $6f_n$. It can be inferred that the effect of rotor–stator interactions significantly influenced the vortex evolution in the volute. The dominant frequency of P6 and P7 was $2.2f_n$ with a relatively low amplitude, which was related to the local flow characteristic caused by flow rate and volute structure. The dominant frequencies of V9 and V10 were $2.2f_n$ and $8.4f_n$, respectively. Compared with other monitoring points, vorticity pulsations frequency components of V9 in the low frequency band were more diverse and of higher amplitude, as it is close to the leading edge of the volute tongue. As V10 was away from the leading edge of the volute tongue, its frequency components of the vorticity pulsations were diverse, and its amplitude was close. This phenomenon was caused by the multiple effects from the flow characteristic of the volute inlet contraction section and impeller inlet. Combining Figures 13–15, it can be concluded that the vorticity fluctuation characteristics in the volute were mainly influenced by the rotor–stator interactions, inlet conditions, and its structure.

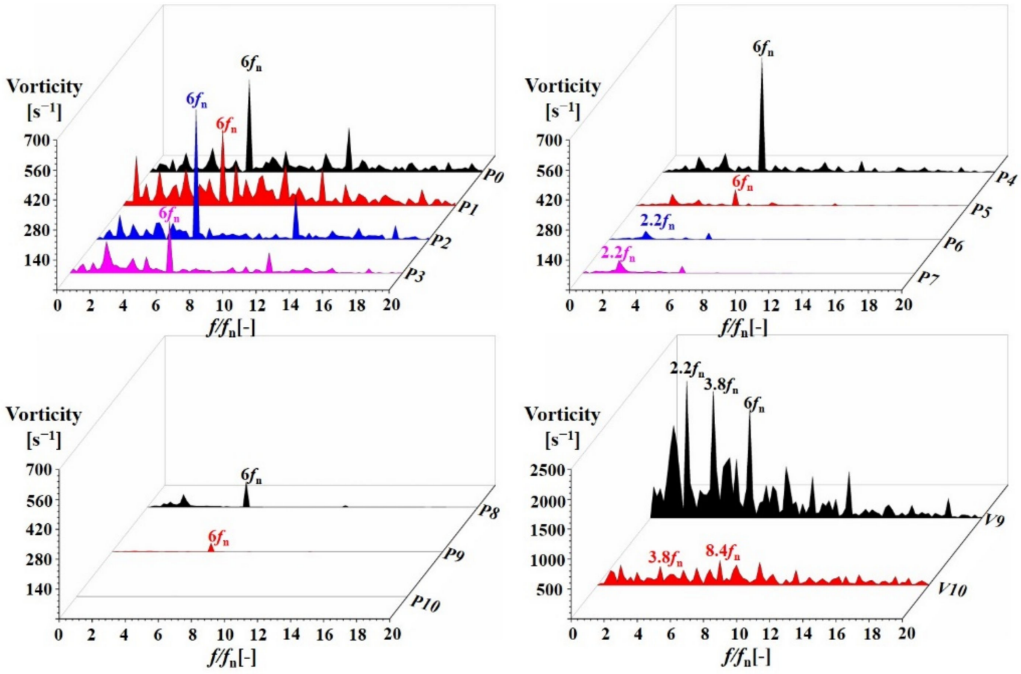

Figure 15. Frequency domain of vorticity fluctuation at the $1.3Q_b$ operation condition.

3.3. Pressure Fluctuation Characteristics

The pressure pulsation intensity coefficient (C_p) was adopted to investigate the impeller rotating affect on the pressure fluctuation characteristics of the volute, which is defined in Equation (14) [38]. The dimensionless parameter C_p is calculated by the standard deviation of pressure in ANSYS CFX 2022 R2. From the definition of C_p, it can be inferred that it is a pressure pulsation statistic of the grid nodes during the statistical period and is independent of the instantaneous state of rotation of the impeller. The lower the value of C_p, the weaker the pressure pulsation intensity in the region during the statistical period. Figure 16 compares the C_p distribution under different operation conditions in the Z = 0 plane of the volute in the last three rotation periods of simulation results. As the flow rate increased, the maximum values of C_p in the Z = 0 plane of the volute increased. However, the high values of C_p regions were in essentially the same position when the flow rate varied, and the C_p concentrated at the small pass-flow section of the volute and the volute outlet. In addition, affected by the rotor–stator interaction, the high values of C_p regions appeared on the tongue side near the runner. The six low values of C_p regions located at the circumferential direction of the volute under the Q_b and $1.3Q_b$ operation conditions aligned with the blade leading edge. It can be concluded that the pressure fluctuation intensity is the lowest in the Z = 0 plane of the volute while the volute tongue aligns with the blade leading edge.

$$C_p = 2\sqrt{\frac{1}{N}\sum_{i-1}^{N-1}(p-\overline{p})^2/\rho u_1^2} \tag{14}$$

where N, i, p, and $\overline{p}$ are the number of time steps, the ith time step, the static pressure at the ith time step, and the average pressure over statistical time, respectively.

As shown in Figure 17, under the Q_b operation condition, the pressure fluctuation of the volute was determined by the effect of the rotor–stator interaction, and its dominant frequency of all monitoring points was the blade pass frequency. The amplitude under the blade pass frequency doubling was relatively large. As the flow cross-section area increased, the local pressure fluctuation amplitude gradually decreased. However, as illustrated in Figure 16, P2 and P6 were located in the low-pressure fluctuation intensity regions and with relatively low-pressure fluctuation amplitudes. As with the vorticity fluctuation

characteristic of P10, its pressure value was constant with the impeller rotation, indicating that the rotor–stator interaction had few effects on the volute inlet contraction section and its upstream section. The monitoring points V9 and V10 were located at the leading edge of the volute tongue with a relatively low and consistent amplitude of pressure fluctuation.

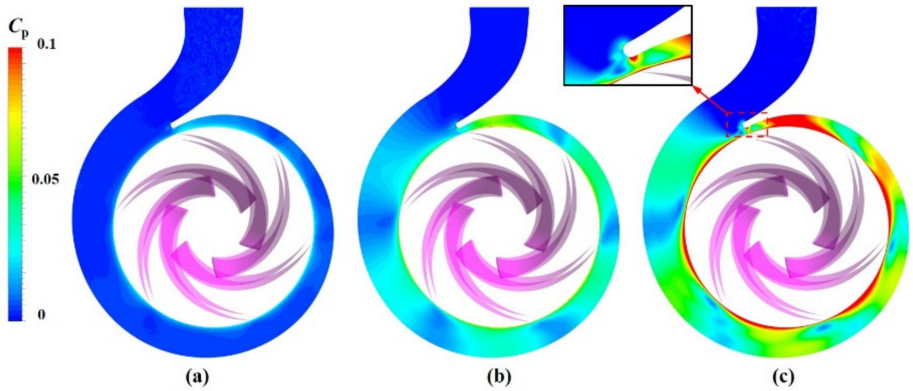

Figure 16. C_p distribution under different operation conditions in the Z = 0 plane of the volute. (**a**) $0.7Q_b$; (**b**) Q_b; (**c**) $1.3Q_b$.

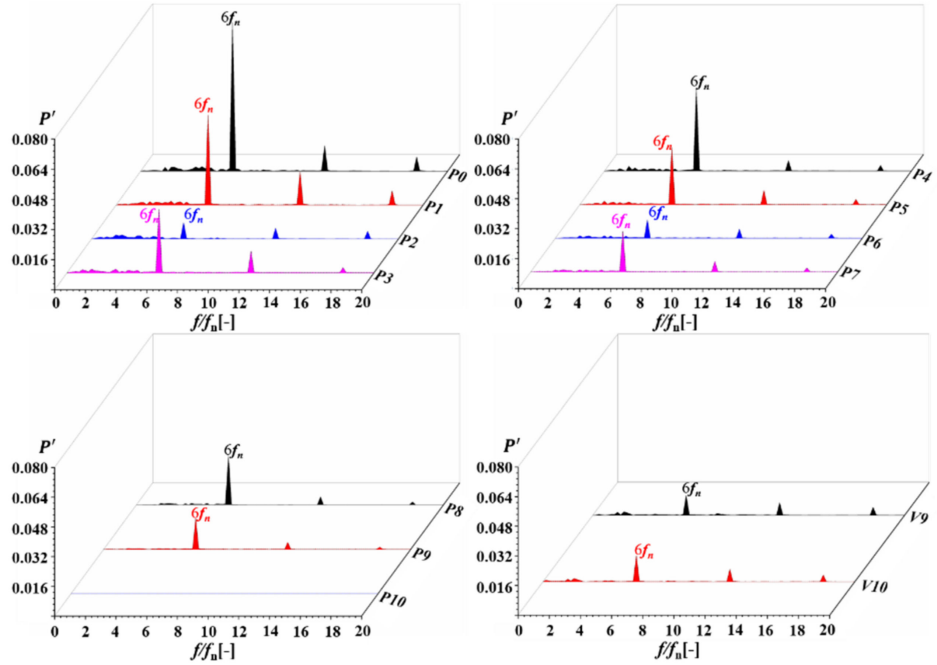

Figure 17. Frequency domain of pressure fluctuation at the Q_b operation condition.

Compared with the Q_b operation condition, the pressure fluctuation amplitude in the volute decreased with the flow rate decrease but with the consistent dominant frequency shown in Figure 18. As the flow section area of the volute decreased, the local fluctuation amplitude and numbers of the high-amplitude frequency components increased. In addition, the pressure fluctuation amplitude was relatively large at the frequency of $0.6f_n$ and $0.8f_n$, indicating that the vortex evolution at the volute circumferential direction had a greater influence on the local pressure fluctuation under the part load condition than the Q_b operation condition. The pressure fluctuation characteristics at the volute tongue leading edge were dominated by the rotor–stator interaction, and the local vortex shedding also increased the fluctuation amplitude at the low-frequency band.

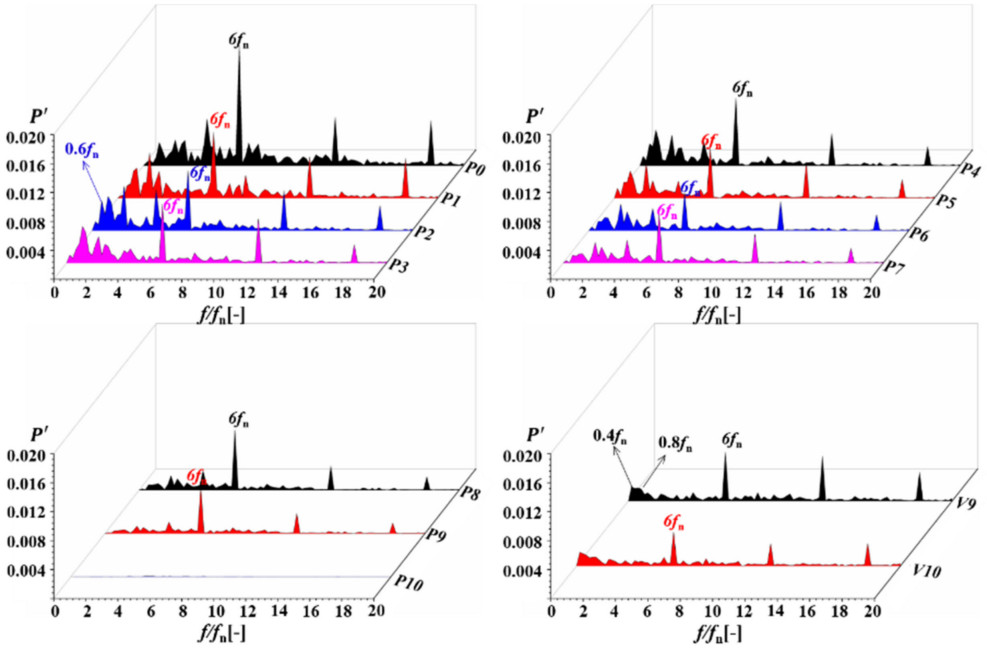

Figure 18. Frequency domain of pressure fluctuation at the $0.7Q_b$ operation condition.

Under $1.3Q_b$ operation conditions, the dominant frequency amplitude of the pressure fluctuation in the volute significantly increased compared with other operation conditions, as shown in Figure 19. The effects of the rotor–stator interaction determined the pressure fluctuation characteristics, but the vortex evolution had a few contributions to causing the local pressure fluctuation in the over load condition. The maximum pressure fluctuation amplitude appeared at P0, which was located in the volute small pass flow section. The pressure fluctuation dominant frequency of V9 and V10 was $6f_n$, and its pressure fluctuation amplitude was relatively large at the frequency of $2.2f_n$ and $3.8f_n$. Combining Figures 18 and 19, a pressure fluctuation frequency of $6f_n$ was generated by the rotor–stator interaction, and $2.2f_n$ and $3.8f_n$ were caused by the vortex periodic shedding from the leading edge of the volute tongue.

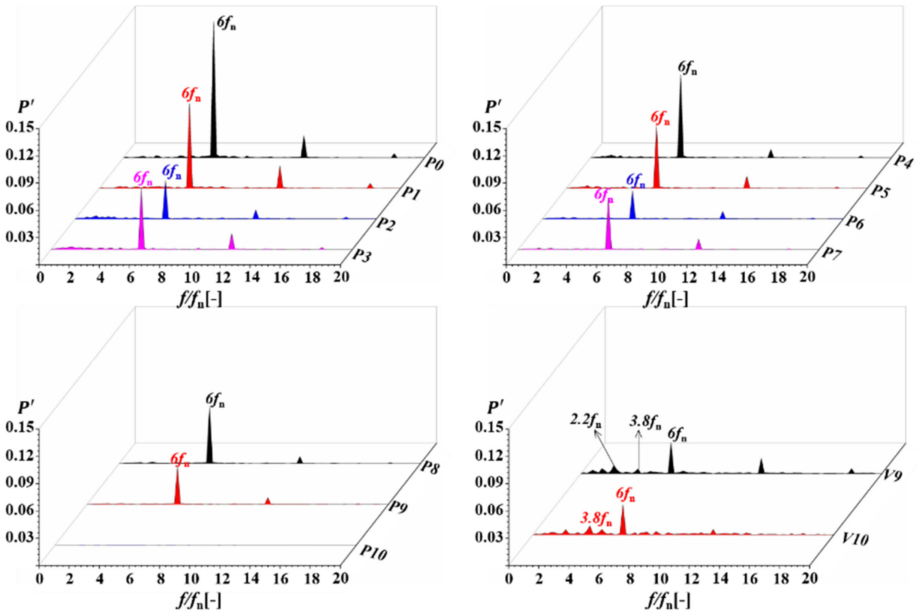

Figure 19. Frequency domain of pressure fluctuation at the $1.3Q_b$ operation condition.

4. Conclusions

The vorticity–pressure fluctuation interaction in the volute of a centrifugal pump as turbines was herein investigated by the numerical method. The accuracy of energy performance and pressure fluctuation characteristic of PATs predicted by the simulation method was verified through the experiment. The vorticity and pressure fluctuation intensity distributions in the volute under different operation conditions were compared. Furthermore, the relationship between vortex evolution with the pressure pulsations in the volute was established by clarify the frequency components corresponding to local high amplitude vorticity and pressure pulsations. The major conclusions can be summarized as follows:

(1) Under Q_b conditions, the effects of impeller rotation had less influence on the vorticity distribution near the volute walls but significantly influenced the vortex evolution at the leading edge of the volute tongue. The evolution of vorticity at the leading edge of the volute tongue intensified the local pressure pulsations as the flow rate increased. Under the different operating conditions of the PATs, the vorticity fluctuation dominant frequency of the volute was significantly varied.

(2) The pressure fluctuation intensity was the lowest in the volute while the volute tongue aligned with the blade leading edge, increasing with the flow rate. The pressure fluctuations characteristic of the volute were dominated by the rotor–stator interaction with the dominant frequency is $6f_n$. The rotor–stator interaction had few effects on the pressure and vorticity fluctuation characteristics of the volute inlet contraction section and its upstream section.

(3) Under Q_b and $1.3Q_b$ conditions, the vorticity pulsation near the wall in the circumferential direction of the volute had less effect on local pressure pulsation characteristics. The effects of impeller rotation had less influence on vortex evolution at the leading edge of the volute tongue under the off-design conditions. The evolution of vorticity at the leading edge of the volute tongue intensified the local pressure pulsations as the flow rate increased. Under the $0.7Q_b$ conditions, the vorticity pulsation characteristics in the volute were complex and had a relatively significant influence on local pressure pulsation.

Author Contributions: Conceptualization, T.L.; methodology, T.L. and X.L.; software, T.L. and Z.Z.; validation, Z.Z.; analysis, T.L.; investigation, T.L. and J.Z.; resources, T.L. and X.L.; writing—review and editing, T.L., J.Z. and J.L.; visualization, Z.Z.; supervision, Z.Z. and X.L.; project administration, Z.Z. and X.L. All authors have read and agreed to the published version of the manuscript.

Funding: This work was supported by the National Natural Science Foundation of China (Grant No. U2006221, 51976197), the Science and Technology Research Project of Jiangxi Provincial Department of Education (Grant No. GJJ214903, GJJ214901), the high-level talent research start-up project of Jiangxi College of Applied Technology (Grant No. JXYY-G2022002).

Data Availability Statement: All the data is already in the article.

Conflicts of Interest: The authors declare no conflict of interest.

Nomenclature

H	Head (m)
Q	Flow rate ($m^3 \cdot s^{-1}$)
N	Total number of cells
φ_{ext}	Extrapolated parameter value (−)
G_{fine}	Fine-grid convergence index (−)
e_{ext}	Extrapolated relative error (−)
e_a	Approximate relative error (−)

p_1	Inlet static pressure of the PAT (Pa)
p_2	Outlet static pressure of the PAT (Pa)
f_n	Impeller rotation frequency (Hz)
C_p	pressure pulsation intensity coefficient (−)
ω_z	Z-direction vorticity (s^{-1})
S_x	Standard deviation (−)
U_R	Random uncertainty (−)
ρ	Density ($kg \cdot m^{-3}$)
η	Efficiency (−)
P'	Pressure fluctuations coefficient (−)
Q_b	Best efficiency flow rate point ($m^3 \cdot s^{-1}$)
n_s	Designed specific speed (−)
T	Torque of the impeller ($N \cdot m^{-1}$)
n	Rotational speed (min^{-1})
y+	y plus value (−)

Abbreviations

PAT	Pump as turbine
RMS	Root mean square
BEP	Best efficiency point
GCI	Grid convergence index
ECD	Electric eddy current dynamometer
CFD	Computational fluid dynamics
BPF	Blade passing frequency
PS	Pressure side of the blade
SS	Suction side of the blade
FDR	Flow deviation ratio

References

1. Zhang, Z.; Su, X.; Jin, Y.; Zhu, Z.; Lin, T. Research on energy recovery through hydraulic turbine system in marine desulfurization application. *Sustain. Energy Technol. Assess.* **2022**, *51*, 101912. [CrossRef]
2. Lin, T.; Zhu, Z.; Li, X.; Li, J.; Lin, Y. Theoretical, experimental and numerical methods to predict the best efficiency point of centrifugal pump as turbine. *Renew. Energy* **2021**, *168*, 31–44. [CrossRef]
3. Lin, T.; Li, X.; Zhu, Z.; Xie, J.; Li, Y.; Yang, H. Application of enstrophy dissipation to analyze energy loss in a centrifugal pump as turbine. *Renew. Energy* **2021**, *163*, 41–55. [CrossRef]
4. Cui, B.; Li, X.; Rao, K.; Jia, X.; Nie, X. Analysis of unsteady radial forces of multistage centrifugal pump with double volute. *Eng. Comput.* **2018**, *35*, 1500–1511. [CrossRef]
5. Huang, S.; Qiu, G.; Su, X.; Chen, J.; Zou, W. Performance prediction of a centrifugal pump as turbine using rotor-volute matching principle. *Renew. Energy* **2017**, *108*, 64–71. [CrossRef]
6. Tao, Y.; Yuan, S.; Liu, J.; Zhang, F. Influence of cross-sectional flow area of annular volute casing on transient characteristics of ceramic centrifugal pump. *Chin. J. Mech. Eng.* **2019**, *32*, 1–13. [CrossRef]
7. Tahani, M.; Kandi, A.; Moghimi, M.; Houreh, S.D. Rotational speed variation assessment of centrifugal pump-as-turbine as an energy utilization device under water distribution network condition. *Energy* **2020**, *213*, 118502. [CrossRef]
8. Štefan, D.; Rossi, M.; Hudec, M.; Rudolfa, P.; Nigrob, A.; Renzi, M. Study of the internal flow field in a pump-as-turbine (PaT): Numerical investigation, overall performance prediction model and velocity vector analysis. *Renew. Energy* **2020**, *156*, 158–172. [CrossRef]
9. Mohammadi, M.; Yasi, M.; Jamali, S.; Hajikandi, H. Experimental Study on Single-and Multi-Stage Pump as Turbine on Water Supply Pipelines. *Iran. J. Sci. Technol. Trans. Civ. Eng.* **2022**, *46*, 3307–3318. [CrossRef]
10. Wang, T.; Wang, C.; Kong, F.; Gou, Q.; Yang, S. Theoretical, experimental and numerical study of special impeller used in turbine mode of centrifugal pump as turbine. *Energy* **2017**, *130*, 473–485. [CrossRef]
11. Wang, T.; Kong, F.; Xia, B.; Bai, Y.; Wang, C. The method for determining blade inlet angle of special impeller using in turbine mode of centrifugal pump as turbine. *Renew. Energy* **2017**, *109*, 518–528. [CrossRef]
12. Su, X.; Huang, S.; Zhang, X.; Yang, S. Numerical research on unsteady flow rate characteristics of pump as turbine. *Renew. Energy* **2016**, *94*, 488–495. [CrossRef]
13. Morabito, A.; Vagnoni, E.; Di Matteo, M.; Hendrick, P. Numerical investigation on the volute cutwater for pumps running in turbine mode. *Renew. Energy* **2021**, *175*, 807–824. [CrossRef]

14. Arani, H.A.; Fathi, M.; Raisee, M.; Nourbakhsh, S.A. Numerical investigation of tongue effects on pump performance in direct and reverse modes. In *IOP Conference Series: Earth and Environmental Science*; IOP Publishing: Bristol, UK, 2019; Volume 240, p. 042003.
15. Arani, H.A.; Fathi, M.; Raisee, M.; Nourbakhsh, S.A. The effect of tongue geometry on pump performance in reverse mode: An experimental study. *Renew. Energy* **2019**, *141*, 717–727. [CrossRef]
16. Qian, Z.; Wang, F.; Guo, Z.; Lu, J. Performance evaluation of an axial-flow pump with adjustable guide vanes in turbine mode. *Renew. Energy* **2016**, *99*, 1146–1152. [CrossRef]
17. Xin, T.; Wei, J.; Qiuying, L.; Hou, G.; Ning, Z.; Yuchuan, W.; Diyi, C. Analysis of hydraulic loss of the centrifugal pump as turbine based on internal flow feature and entropy generation theory. *Sustain. Energy Technol. Assess.* **2022**, *52*, 102070. [CrossRef]
18. Lu, Z.; Xiao, R.; Tao, R.; Li, P.; Liu, W. Influence of guide vane profile on the flow energy dissipation in a reversible pump-turbine at pump mode. *J. Energy Storage* **2022**, *49*, 104161. [CrossRef]
19. Giosio, D.R.; Henderson, A.D.; Walker, J.M.; Brandnerb, P.A.; Sargisonc, J.E.; Gautam, P. Design and performance evaluation of a pump-as-turbine micro-hydro test facility with incorporated inlet flow control. *Renew. Energy* **2015**, *78*, 1–6. [CrossRef]
20. Shi, F.X.; Yang, J.H.; Wang, X.H. Analysis on the effect of variable guide vane numbers on the performance of pump as turbine. *Adv. Mech. Eng.* **2018**, *10*, 1687814018780796. [CrossRef]
21. Zhang, L.; Davila, G.; Zangeneh, M. Multi-objective optimization of a high specific speed centrifugal volute pump using three-dimensional inverse design coupled with computational fluid dynamics simulations. *J. Fluids Eng.* **2021**, *143*, 021202. [CrossRef]
22. Shim, H.S.; Kim, K.Y. Design optimization of the impeller and volute of a centrifugal pump to improve the hydraulic performance and flow stability. *J. Fluids Eng.* **2020**, *142*, 10. [CrossRef]
23. Shim, H.S.; Kim, K.Y. Effects of the cross-sectional area of a volute on suction recirculation and cavitation in a centrifugal pump. *J. Fluids Eng.* **2020**, *142*, 5. [CrossRef]
24. Morros, C.S.; Oro, J.M.F.; Díaz, K.M.A. Numerical modelling and flow analysis of a centrifugal pump running as a turbine: Unsteady flow structures and its effects on the global performance. *Int. J. Numer. Methods Fluids* **2011**, *65*, 542–562. [CrossRef]
25. Binama, M.; Su, W.T.; Cai, W.H.; Lic, X.-B.; Muhirwaa, A.; Lia, B.; Bisengimana, E. Blade trailing edge position influencing pump as turbine (PAT) pressure field under part-load conditions. *Renew. Energy* **2019**, *136*, 33–47. [CrossRef]
26. Xiang, R.; Wang, T.; Fang, Y.; Yu, H.; Zhou, M.; Zhang, X. Effect of blade curve shape on the hydraulic performance and pressure pulsation of a pump as turbine. *Phys. Fluids* **2022**, *34*, 085130. [CrossRef]
27. Yang, S.S.; Kong, F.Y.; Qu, X.Y.; Jiang, W.M. Influence of blade number on the performance and pressure pulsations in a pump used as a turbine. *J. Fluids Eng.* **2012**, *134*, 12. [CrossRef]
28. Buono, D.; Frosina, E.; Mazzone, A.; Cesaro, U.; Senatore, A. Study of a pump as turbine for a hydraulic urban network using a tridimensional CFD modeling methodology. *Energy Procedia* **2015**, *82*, 201–208. [CrossRef]
29. Gao, Y.; Fan, X.; Dang, R. Numerical characterization of the effects of flow rate on pressure and velocity distribution of pump as turbine. *Curr. Sci.* **2019**, *117*, 00113891. [CrossRef]
30. Fei, Z.; Zhang, R.; Xu, H.; Feng, J.; Mu, T.; Chen, Y. Energy performance and flow characteristics of a slanted axial-flow pump under cavitation conditions. *Phys. Fluids* **2022**, *34*, 035121. [CrossRef]
31. Lin, Y.; Li, X.; Zhu, Z.; Wang, X.; Lin, T.; Cao, H. An energy consumption improvement method for centrifugal pump based on bionic optimization of blade trailing edge. *Energy* **2022**, *246*, 123323. [CrossRef]
32. Wu, C.; Pu, K.; Li, C.; Wu, P.; Huang, B.; Wu, D. Blade redesign based on secondary flow suppression to improve energy efficiency of a centrifugal pump. *Energy* **2022**, *246*, 123394. [CrossRef]
33. Ji, L.; Li, W.; Shi, W.; Chang, H.; Yang, Z. Energy characteristics of mixed-flow pump under different tip clearances based on entropy production analysis. *Energy* **2020**, *199*, 117447. [CrossRef]
34. Zhang, F.; Appiah, D.; Hong, F.; Zhang, J.; Yuan, S.; Adu-Poku, K.A.; Wei, X. Energy loss evaluation in a side channel pump under different wrapping angles using entropy production method. *Int. Commun. Heat Mass Transf.* **2020**, *113*, 104526. [CrossRef]
35. Spalart, P.R.; Shur, M. On the sensitization of turbulence models to rotation and curvature. *Aerosp. Sci. Technol.* **1997**, *1*, 297–302. [CrossRef]
36. Roache, P.J. Quantification of uncertainty in computational fluid dynamics. *Annu. Rev. Fluid Mech.* **1997**, *29*, 123–160. [CrossRef]
37. Celik, I.B.; Ghia, U.; Roache, P.J.; Freitas, C.J. Procedure for estimation and reporting of uncertainty due to discretization in CFD applications. *J. Fluids Eng.-Trans. ASME* **2008**, *130*, 078001. [CrossRef]
38. Yang, B.; Li, B.; Chen, H.; Liu, Z.; Xu, K. Numerical investigation of the clocking effect between inducer and impeller on pressure pulsations in a liquid rocket engine oxygen turbopump. *J. Fluids Eng.* **2019**, *141*, 071109. [CrossRef]